



HAL
open science

Radiant fraction from sooting jet fires

Fatiha Nmira, Jean-Louis Consalvi, M.A. Delichatsios

► **To cite this version:**

Fatiha Nmira, Jean-Louis Consalvi, M.A. Delichatsios. Radiant fraction from sooting jet fires. *Combustion and Flame*, 2019, 208, pp.51-62. hal-02971308

HAL Id: hal-02971308

<https://hal.science/hal-02971308>

Submitted on 25 Oct 2021

HAL is a multi-disciplinary open access archive for the deposit and dissemination of scientific research documents, whether they are published or not. The documents may come from teaching and research institutions in France or abroad, or from public or private research centers.

L'archive ouverte pluridisciplinaire **HAL**, est destinée au dépôt et à la diffusion de documents scientifiques de niveau recherche, publiés ou non, émanant des établissements d'enseignement et de recherche français ou étrangers, des laboratoires publics ou privés.



Distributed under a Creative Commons Attribution - NonCommercial 4.0 International License

Radiant fraction from sooting jet fires

F. Nmira^{*}, J.L. Consalvi^{**,†}, M.A. Delichatsios^{***}

^{*} Direction R&D EDF, 6 quai Watier, 78400 Chatou, France.

^{**} Aix-Marseille Université, CNRS, IUSTI UMR 7343, 5 rue E. Fermi, 13013 Marseille, France.

^{***} Visiting Professor Northeastern University, Boston, USA

[†] *Corresponding author*: Tel.: +33 491-106-831; Fax: +33-491-106-969.

E-mail address: jean-louis.consalvi@univ-amu.fr

Abstract :

The objective of this article is to investigate numerically the radiative structure of methane, ethylene and acetylene lab-scale jet flames ranging from the transitional to the momentum-driven regimes. The numerical model involves a hybrid flamelet/transported PDF method coupled to an acetylene-benzene soot production model and a Wide-Band Correlated-K gas radiation model. Model predictions in terms of mean and rms soot volume fraction and temperature, integrated soot volume fraction and radiant fraction are in reasonable agreement with the available experimental data. In particular, the model reproduces quantitatively the decrease in radiant fraction observed as the flow becomes momentum driven. This behavior results mainly from two mechanisms: i) an increase in flame self-absorption due to an enhancement in flame volume and ii) for the ethylene and acetylene flames a reduction in the soot emission per unit flame volume owing to a strong decrease in soot production. In addition, for a given fuel, gas emission per unit flame volume remains approximately constant as the exit strain rate increases whereas the soot emission per unit flame volume and the characteristic soot volume fraction scale with the Kolmogorov time scale. It was also

found that competitive mechanisms govern the effects of Turbulence-Radiation Interaction (TRI) on radiant fraction. Enhancement mechanisms are due to gas emission TRI and temperature self-correlation effects on soot emission whereas inhibiting mechanisms results from the negative correlation between soot volume fraction and temperature. Enhancement mechanisms dominate in weakly sooting methane flames and taking TRI into account increases the radiant fraction. On the other hand, inhibiting mechanisms become significant in moderately and highly sooting fuels, with their importance increasing with both the fuel sooting propensity and the Reynolds number. For flames dominated by soot radiation, the inhibiting mechanisms prevail and taking TRI into account reduces the radiant fraction.

Key Words: Sooting jet fires, transported PDF method, radiant fraction, turbulence effects, turbulence-radiation interactions.

Nomenclature

A_S	soot surface area [m^{-1}]
C_a	agglomeration rate constant [-]
C_{min}	number of carbon atoms in the incipient soot particle [-]
d_F	inner burner diameter [m]
F_r	Froude number [-]
f_S	soot volume fraction [-]
$f_{S,EQ}$	equivalent soot volume fraction [-]
G_η	incident radiation per unit wavenumber [$\text{W}\cdot\text{m}^{-1}$]
h	enthalpy [$\text{J}\cdot\text{kg}^{-1}$]
L_{fl}	stoichiometric flame height [m]
I_b	spectrally-integrated blackbody intensity [W m^{-2}]
$I_{b\eta}$	blackbody intensity at wavenumber η [W m^{-1}]

k_B	Boltzmann constant [$\text{J}\cdot\text{kg}^{-1}$]
N_a	Avogadro number [$\text{part}\cdot\text{mol}^{-1}$]
N_S	soot number density per unit mass of mixture [$\text{part}\cdot\text{kg}^{-1}$]
P_{O_2}	partial pressure of O_2 [Pa]
P_{OH}	partial pressure of OH [Pa]
\dot{Q}	heat release rate [W]
\dot{Q}_{abs}	total absorption [W]
\dot{Q}_{em}	total emission [W]
\dot{Q}_{em}'''	total emission per unit flame volume [W m^{-3}]
$\dot{Q}_{em,g}'''$	gas emission per unit flame volume [W m^{-3}]
$\dot{Q}_{em,s}'''$	soot emission per unit flame volume [W m^{-3}]
r	radial coordinate [m]
Re	injection Reynolds number [-]
t_{res}	residence time of the fuel in the flame envelop [s]
t_{Kol}	Kolmogorov time scale [s]
T	temperature [K]
U_F	fuel injection velocity [$\text{m}\cdot\text{s}^{-1}$]
V	volume [m^3]
V_{fl}	flame volume [m^3]
W_S	soot molecular weight [$\text{kg}\cdot\text{mol}^{-1}$]
W_{fl}	flame width [m]
X_R	enthalpy defect parameter [-]
Y_S	soot mass fraction [-]
z	axial coordinate [m]
Z_{st}	stoichiometric mixture fraction [-]

χ	scalar dissipation rate [s^{-1}]
χ_{em}	emission fraction [-]
χ_R	radiant fraction [-]
Δh_c	heat of combustion [$J\ kg^{-1}$]
φ_i	collision efficiency factor of the i^{th} species [-]
η	wavenumber [cm^{-1}]
κ_η	absorption coefficient at wavenumber η [$m^{-1}\ cm^{-1}$]
κ_P	Planck- mean absorption coefficient [m^{-1}]
$\kappa_{Pg,EQ}$	Planck- mean absorption coefficient for gas at equilibrium composition [m^{-1}]
ρ	density [$kg\cdot m^{-3}$]
ρ_S	soot density [$kg\cdot m^{-3}$]
$\dot{\omega}_c$	reaction rate for coagulation [$mol\cdot m^{-3}\cdot s^{-1}$]
$\dot{\omega}_n$	reaction rate for soot nucleation [$mol\cdot m^{-3}\cdot s^{-1}$]
$\dot{\omega}_{sg}$	reaction rate for soot surface growth [$mol\cdot m^{-3}\cdot s^{-1}$]
$\dot{\omega}_{NS}$	reaction rate for soot number density [$part\cdot m^{-3}\cdot s^{-1}$]
$\dot{\omega}_{O_2}$	reaction rate for soot oxidation by O_2 [$kg\cdot m^{-3}\cdot s^{-1}$]
$\dot{\omega}_{OH}$	reaction rate for soot oxidation by OH [$kg\cdot m^{-3}\cdot s^{-1}$]
$\dot{\omega}_{Y_S}$	source term for soot mass fraction [$kg\cdot m^{-3}\cdot s^{-1}$]
ζ	mixture fraction [-]

Subscript

abs	absorption
c	agglomeration
EQ	equilibrium
em	emission

F	fuel
<i>fl</i>	flame
g	gas
P	<i>Planck</i>
R	radiation or radiative
S	soot
η	at a given wavenumber or per unit wavenumber

1. Introduction

Radiation from turbulent jet diffusion flames is a recurrent problem in fire safety engineering as well as in industry. This has motivated a significant amount of experimental studies to characterize the radiative heat transfer (RHT) in ‘non-luminous’ and luminous lab- or large scale turbulent jet flames [1-9]. Among the parameters that characterize the RHT in jet flames, the radiant fraction, χ_R , defined as the part of the heat release rate radiated away from the flame, is of particular interest since it quantifies the radiant power transferred to the environment. In the case of ‘non-luminous’ lab- and large scale jet flames, Molina et al. [10] suggested that χ_R can be related to a global residence time, t_{res} , and an emission term characterizing the fuel. The description in [10] was revisited in Ref. [11] where it was found that χ_R can be expressed as $\chi_R \propto t_{res} \dot{Q}_{em}''' (1 - \dot{Q}_{abs}/\dot{Q}_{em})$ where \dot{Q}_{em}''' is the total emission per unit flame volume and $\dot{Q}_{abs}/\dot{Q}_{em}$ is the ratio of total absorption to total emission which introduces the flame self-absorption. Delichatsios and Orloff [3] considered methane, propylene and acetylene turbulent jet flames ranging from buoyancy to momentum controlled conditions. For a given fuel and nozzle diameter, the exit strain rate was increased through an enhancement of the fuel injection velocity, resulting in a decrease in χ_R . The rate of decrease

was found to be higher in the high-sooting propylene and acetylene flames than in the low-sooting methane flames. In addition, they concluded that the Kolmogorov time scale controls the soot formation based on a scaling analysis of the experimental data for the case where soot was the dominant source of radiation.

Numerical modelling of RHT in non-sooting or sooting turbulent flames has made significant progress over the last twenty years [12] owing to, on the one hand, the emergence of accurate high-temperature spectroscopic database, such as HITEMP 2010 [13], and reliable radiative property models based on the k-distribution concept [14] and, on the other hand, to the development of efficient RTE solvers such as the Discrete Ordinates Method, the Finite Volume Method, the high-order PN and the Monte Carlo [14]. In addition, the application of Transported PDF methods allowed to describe accurately the strong coupling between turbulence and radiation which affects significantly the RHT in turbulent flames [12]. These advanced radiation models have contributed to providing a better understanding of the turbulence-radiation interactions (TRI) in both non-luminous and luminous flames [15-23].

The main objective of this study is to provide a better understanding of the radiative structure of sooting jet fires by using a Wide Band Correlated-k (WBCK) method coupled to a transported PDF approach to model emission TRI. It extends the methodology and analysis developed in Ref. [11] for non-luminous jet flames to luminous jet flames. Methane, ethylene and acetylene fuels, characterized by weak, moderate and high-sooting propensity, respectively, will be considered. The turbulence will be varied by using a strategy similar to that proposed by Delichatsios and Orloff [3]. The article is organized as follows. The numerical model is presented in section 2 after which results are discussed in section 3. Finally section 4 contains the concluding remarks drawn from the present study.

2. Numerical model

The turbulent jet diffusion flames are modelled by using the physical models and numerical algorithms described in detail in Ref. [24]. This model is based on a hybrid flamelet/transported PDF method which allows capturing turbulence/soot production interaction and turbulence/radiation interaction. This approach, coupled to a two-equation acetylene-benzene soot production model and a Wide-Band Correlated-K radiative property model was intensively validated in terms of flame structure, soot production and radiative outputs in C₁-C₃ jet diffusion flames covering wide ranges of Reynolds number, residence time, fuel sooting propensity, oxygen-enhanced oxidizer and moderate increases in pressure [24, 25].

The Favre-Averaged Navier-Stokes equations are solved in axisymmetric cylindrical coordinates in connection with the k-ε model with the standard set of constants, except $C_{\varepsilon 1}$ that was set equal to 1.5. The enthalpy defect flamelet model is used to obtain state relationships for density, species and temperature as unique functions of mixture fraction, ζ , scalar dissipation rate, χ , and enthalpy defect, $h - h_{ad}$ where h_{ad} is the adiabatic enthalpy [24]. The flamelet library was generated by using the mechanism of Qin et al. [26].

The acetylene/benzene-based two-equation soot model, proposed by Lindstedt [27], was used coupled to the models of Nagle and Strickland-Constable (NSC) [28] and Fenimore and Jones [28] for soot oxidation by O₂ and OH, respectively. In this model soot primary particles are assumed to be spherical and locally monodisperse. Under such conditions soot properties can be described in terms of soot number density of primary particles, ρN_S , and soot mass fraction, Y_S . The source terms and model constants for soot number density, $\dot{S}_N = N_a/C_{min} \dot{\omega}_n - \dot{\omega}_c$, and soot mass fraction, $\dot{S}_{Y_S} = (\dot{\omega}_n + \dot{\omega}_{sg})W_S - \dot{\omega}_{O_2} - \dot{\omega}_{OH}$, are given in Table 1.

The radiation model was described in detail in Ref. [24]. The spectral coverage range considered in the present study is 200-9200 cm^{-1} . The radiatively participating species considered are CO_2 , H_2O , and soot. The Rayleigh's theory was applied to obtain the soot absorption coefficient with the refractive and absorptive indexes of the soot determined using the correlations of Chang and Charalampopoulos [30]. A wide-band (WB) correlated-k model was used as the radiative property model. The spectrum was divided into $N_{WB}=14$ WBs with a spectral resolution of $\Delta\eta_{WB}=500 \text{ cm}^{-1}$. On each wide band WB k-g distributions were assembled from a narrow band (NB) database, generated from HITEMP 2010 [13], by using a lumping strategy [31]. The gas mixture was treated at the narrow band (NB) level by using the mixing scheme developed by Modest and Riazzi [32]. Integrations over the g-space were performed by using a Gauss quadrature scheme with 4 points. The WB RTE was solved by using the Finite Volume Method [33]. Concerning turbulence-radiation interaction, absorption TRIs are accounted for by using the Optically-thin fluctuation approximation (OTFA) and emission TRI is modelled 'exactly' by using a joint composition PDF [24].

Based on previous studies, the scalar dissipation rate is assumed to be statistically independent of the other scalars and its PDF is modelled by a Dirac function [24]. The default set of composition variables is therefore $\underline{\phi} = \{\zeta, X_R, N_S, Y_S\}$. A gradient transport model for turbulent velocity fluctuations and the Interaction by Exchange with the Mean (IEM) model are considered to close both turbulent diffusion and micro-mixing terms [24]. The joint composition PDF transport is solved using the Stochastic Eulerian Field method with 60 fields [34].

3. Results and discussions

3.1. Experimental data and computational details

The numerical simulations are mainly based on the experiments of Delichatsios and Orloff [3] who measured radiant fractions in methane, acetylene and propylene diffusion flames. In the framework of this study, only methane and acetylene, which are weakly- and highly-sooting fuels, respectively, will be considered. Propylene has a sooting propensity similar to that of acetylene and will not be considered. In order to complete this set of data, simulations will be run by using ethylene, a moderately-sooting fuel.

The experimental conditions are summarized in Table 2, including the fuel exit velocity, U_F , the fuel nozzle diameter, d_F , the exit strain rate, U_F/d_F , which is proportional to the large scale flame residence time for momentum controlled jets [3], the Reynold number, Re , the heat release rate (HRR), \dot{Q} , the Froude number, Fr , as defined in Ref. [37] and the Kolmogorov time scale, t_{Kol} , estimated as $\sqrt{\nu_F L_{fl}/U_F^3}$ following Ref. [3]. In this latter expression, ν_F and L_{fl} are the fuel kinematic viscosity and the flame height, respectively. The flame length, L_{fl} and width, W_{fl} , are defined based on the iso-contour 1400K. This value was selected since it is expected to correspond to a threshold below which soot ceases to be oxidized [35, 36], being then representative of the “luminous” flame. Table 2 shows that the flames belong either to the momentum-driven regime ($Fr > 5$) or to the transitional regime between the momentum-driven and buoyancy-driven regimes ($Fr < 5$) [37]. For each fuel, three nozzle diameters are considered. For each nozzle diameter the exit strain rate, the HRR and the fuel exit Reynolds number are enhanced by increasing the fuel injection velocity, leading in turns to a decrease in the Kolmogorov time scale. It should be pointed out that some ethylene flames produced by a 2.18 mm-diameter nozzle were investigated experimentally by Lee et al. [38] and will serve to validate the model.

For the flames generated by nozzle diameters of 1 and 2 mm, a computational domain with a size of 0.1m (r) \times 1m (z) was used. The computational domain was extended to 0.15m (r) \times 1.25 m (z) for the flames produced by a nozzle diameter of 3 mm. Non-uniform meshes with 54 (r) \times 93 (z) and 69 (r) \times 113 (z) cells were considered, respectively. In both cases, a uniform mesh was used in the flaming region with a grid size of 1cm \times 1cm. This was found to be sufficient to achieve grid-independent solutions.

3.2. Comparison with available data

The capability of the numerical model to reproduce the effects of exit strain rate on soot production will be assessed by comparison with the experimental data obtained by Lee et al. [38]. Ethylene jet flames were generated by a 2.18 mm-diameter nozzle. The fuel injection Reynolds number was enhanced from 4000 to 23200 by increasing the fuel exit velocity, similarly to the procedure used by Delichatsios and Orloff [3]. In a previous study [24], the present numerical model was found to reproduce reasonably the experimental data in terms of axial and radial profiles of mean and rms temperature and soot volume fraction (SVF) for the flame with a Reynolds number of 12000. For more details concerning this particular comparison, the reader can refer to Ref. [24].

Figure 1 shows that, as the Reynolds number (or U_F/d_F) is increased, the peaks of mean and rms SVF occurs approximately at the same location whereas their magnitude is reduced. These trends are captured quantitatively by the numerical model, although the peak values are systematically overpredicted.

Figure 2 shows the radial profiles of mean SVF at different axial locations. $z/d_F = 60, 90$ and 120 are located within the soot growth region, $z/d_F = 150$ corresponds approximately to the location of maximum SVF whereas $z/d_F = 180$ is within the soot oxidation region. The

radial profiles are on the whole in reasonable agreement with the experimental data despite a systematic overprediction. The experimental data in Fig. 2 shows also that increasing the Reynolds number leads to broader radial profiles whereas the SVF decreases at a given axial location. These behaviours are well reproduced by the model.

Figure 3 shows the axial evolution of the integrated SVF, defined as $2\pi \int f_s r dr$. As discussed by Lee et al. [38], the integrated SVF is weakly influenced by the Reynolds number, except for the $Re = 4000$ flame which exhibits integrated SVF significantly lower than for the other Reynolds numbers. These trends are also reproduced quantitatively by the numerical model.

Figure 4 displays the evolution of the radiant fraction, $\chi_R = (\dot{Q}_{em} - \dot{Q}_{abs})/\dot{Q}$, as a function of the HRR and U_F/d_F . $\dot{Q}_{em} = \int_V \int_\eta 4\pi \langle \kappa_\eta I_{b\eta} \rangle d\eta dV = \int_V 4\pi \langle \kappa_p I_b \rangle dV$ is the total emission and $\dot{Q}_{abs} = \int_V \int_\eta \langle \kappa_\eta \rangle \langle G_\eta \rangle d\eta dV$ is the total absorption. Figure 4 shows that, for a given fuel, the radiant fractions exhibit an asymptotic behavior for the flames with the lowest HRR (and U_F/d_F). These flames are the most influenced by the buoyancy forces among the set of data considered. As discussed by Delichatsios and Orloff [3], the asymptotic values of χ_R correspond approximately to the radiant fraction of turbulent buoyant jets. For given fuel and nozzle diameter, the radiant fraction decreases as the HRR (or U_F/d_F) increases and this behavior is more pronounced for the moderately-sooting ethylene flames and the highly-sooting acetylene flames than for the weakly-sooting methane flames. Model predictions are on the whole within 20% of the experimental data. The largest discrepancies are observed for the methane flames.

3.3. Data analysis

3.3.1. Theoretical background

Following Ref. [11], the radiant fraction can be conveniently expressed for analysis as:

$$\chi_R = \frac{\dot{Q}_{em}}{\dot{Q}} \left(1 - \frac{\dot{Q}_{abs}}{\dot{Q}_{em}} \right) = \chi_{em} \left(1 - \frac{\dot{Q}_{abs}}{\dot{Q}_{em}} \right) \quad (1)$$

where the ratio of total absorption to total emission, $\dot{Q}_{abs}/\dot{Q}_{em}$, quantifies the flame self-absorption and can be used as a measure of the flame optical thickness. χ_{em} represents the ratio of total emission to HRR and by assuming that most of radiation is emitted within the flame volume, V_{fl} , can be rewritten as:

$$\chi_{em} = \frac{V_{fl}}{U_F d_F^2} \underbrace{\frac{\int_{V_{fl}} 4\pi(\kappa_{p,g} + \kappa_{p,s}) I_b dV}{V_{fl}}}_{\dot{Q}_{em}''' = \dot{Q}_{em,g}''' + \dot{Q}_{em,s}'''} \frac{4}{\pi \rho_F \Delta h_c} \quad (2)$$

V_{fl} is estimated as $V_{fl} = \pi W_{fl}^2 L_{fl} / 12$ in accordance with Ref. [39], assuming that the flame is the sum of two opposite cones, with the diameter and the height of each cone being W_{fl} and $L_{fl}/2$, respectively. $t_{res} = V_{fl}/U_F d_F^2$ is the residence time of the fuel in the flame envelop and, for a given fuel, can be related to the residence defined by Turns and Mhyr [5], i.e. $\tau_G = \rho_{fl} W_{fl}^2 L_{fl} Z_{st} / 3 \rho_F d_F^2 U_F$. $\dot{Q}_{em,g}''' = \int_{V_{fl}} 4\pi \kappa_{p,g} I_b dV / V_{fl}$ and $\dot{Q}_{em,s}''' = \int_{V_{fl}} 4\pi \kappa_{p,s} I_b dV / V_{fl}$ represent the emission of the radiatively participating gaseous species and soot per unit flame volume, respectively. The term $4\dot{Q}_{em}''' / \pi \rho_F \Delta h_c$ can be interpreted as the inverse of a radiation cooling time. It should be pointed out that $4/\pi \rho_F \Delta h_c$ depends only on the fuel. Consequently, for a given fuel, the evolution of radiant fraction with the strain rate can be explained from the contribution of three terms:

$$\chi_R \propto \underbrace{t_{res}}_I \underbrace{(\dot{Q}_{em,g}''' + \dot{Q}_{em,s}''')}_{II} \underbrace{\left(1 - \frac{\dot{Q}_{abs}}{\dot{Q}_{em}} \right)}_{III} \quad (3)$$

The emission per unit flame volume can be further developed as $\dot{Q}_{em}''' \sim \kappa_p \sigma T_R^4$ where κ_p and T_R are effective Planck-mean absorption coefficient, including radiant gases and soot contributions, and radiation temperature, respectively. For sooting flames, the effective radiation temperature is expected to decrease due to radiation cooling effects as the soot volume fraction and, thus, radiative loss increase [40].

3.3.2. Emission fraction

The previous analysis leads to:

$$\chi_{em} \propto t_{res}(\dot{Q}_{em,g}''' + \dot{Q}_{em,s}''') \quad (4)$$

Let us first consider the emission of gas and soot per unit flame volume. The left row of Fig. 5 represents $\dot{Q}_{em,g}'''$ and $\dot{Q}_{em,s}'''$ as a function of the exit strain rate, U_F/d_F . It should be pointed out that U_F/d_F represents the residence time in the flame, assuming momentum-controlled conditions. It can be observed that, for a given fuel, $\dot{Q}_{em,g}'''$ remains approximately constant over the entire range of U_F/d_F whereas $\dot{Q}_{em,s}'''$ decreases by almost two order of magnitudes as U_F/d_F increases. Emission for methane flames is strongly dominated by gas with the contribution of soot emission to the total emission decreasing from about 6.2% for the lowest strain rate to about 0.15% for the highest. For the ethylene flames, gas and soot emissions are on the whole of the same order of magnitude, except for the four flames that are represented by the larger symbols in Fig. 5b₁. It should be pointed out that these flames belong to the momentum-driven regime and are strongly dominated by gas emission. Figure 5b₁ shows also that soot emission prevails on gas radiation for U_F/d_F lower than $2 \times 10^4 \text{ s}^{-1}$. For the acetylene flames, soot emission is one order of magnitude higher than gas emission for the lowest exit strain rates. As U_F/d_F increases, soot emission decreases and the two contributions tend to

become comparable for the highest values of U_F/d_F . The right row in Fig. 5 represents the equivalent soot volume fraction defined as:

$$f_{S,EQ} = \frac{\max(2\pi \int f_S r dr)}{\pi W_{fl}^2} \quad (5)$$

Figure 5 shows that, for given fuel and nozzle diameter, the evolutions of $\dot{Q}_{em,S}'''$ and $f_{S,EQ}$ with U_F/d_F follow similar trends. This is illustrated in Fig. 6 by the almost linear relationship between $\dot{Q}_{em,S}'''$ and $f_{S,EQ}$.

Figures 5 a, b, and c shows that both $\dot{Q}_{em,S}'''$ and $f_{S,EQ}$ are not well correlated when plotted as a function of U_F/d_F , the effects of the nozzle diameter being clearly still persistent. This suggests that soot production and emission are not determined by characteristic time scales based on U_F/d_F . Alternatively, Delichatsios and Orloff [3] suggested that the Kolmogorov time scale, t_{Kol} , is appropriate for these processes. The relevance of this assumption is confirmed in Fig. 7 where, for a given fuel, all the $\dot{Q}_{em,S}'''$ collapse onto a single when plotted as a function of t_{Kol} .

The previous discussion showed that, for a given fuel, $\dot{Q}_{em,g}'''$ remains approximately constant and $\dot{Q}_{em,S}'''$ is a function of the Kolmogorov time scale. This suggests that Eq. 4 can be rewritten as:

$$\frac{\chi_{em}}{t_{res}} = f(t_{Kol}) \quad (6)$$

Figures 8 a to c exhibit this relationship for the three fuels. It can be observed that the dependency of χ_{em}/t_{res} on t_{Kol} increases with the sooting propensity of the fuel. In the case

of methane flames, χ_{em}/t_{res} is almost independent on t_{Kol} due to the weak contribution of soot emission and χ_{em} is a linear function of t_{res} only (see Fig. 8d).

3.3.3. Effective Optical thickness

The left row in Fig. 9 shows the evolution of $\dot{Q}_{abs}/\dot{Q}_{em}$ as a function of U_F/d_F . $\dot{Q}_{abs}/\dot{Q}_{em}$ ranges from about 0.14 to about 0.37, showing that none of these flames can be assumed as optically thin. It can be observed that $\dot{Q}_{abs}/\dot{Q}_{em}$ increases with the strain rate. This increase can be, at least partially, related to an increase in flame size as illustrated in the right row of Fig. 9 that represents the evolution of W_{fl} with U_F/d_F .

Figure 9 shows also that, for given diameter, $\dot{Q}_{abs}/\dot{Q}_{em}$ increases more rapidly with the strain rate for the methane and ethylene flames than for the acetylene flames. These differences in behaviour can be explained from the conclusions drawn by Metha and co-workers [16] who showed that soot is comparatively more transparent than the gaseous radiatively participating species. They investigated emission and absorption of soot and participating gases in weakly and moderately sooting lab-scale jet diffusion flames and reported that a significant part of gas emission (35-55%) was absorbed within the flame by the gases owing to the specific spectral bands of gas absorption whereas less than 10% of soot radiation was absorbed within the flame by soot due to the continuum nature of soot radiation. In methane and ethylene flames, the contribution of gas radiation is significant and, as a consequence, the most important part of absorption is expected to be due to the gases, although this part is expected to be lower in ethylene flames. In the case of acetylene flames, radiation is mainly due to soot. On the one hand, soot is relatively more transparent than gaseous participating species as discussed previously and, on the other hand, SVF decreases when increasing the strain rate. Both effects limit the increase in absorption with the flame size (and U_F/d_F), explaining the observed differences with the methane and ethylene flames.

$\dot{Q}_{abs}/\dot{Q}_{em}$ was found to be correlated as a function of $\kappa_{pg,EQ}W_{fl}$ for ‘non-luminous’ hydrogen and methane jet flames [11], where $\kappa_{pg,EQ}$ is the Planck-mean absorption coefficient of the radiatively participating gaseous species evaluated by assuming an adiabatic flame temperature and an equilibrium composition [10]. $\kappa_{pg,EQ}$ was computed from HITEMP 2010 [13]. The previous discussion suggests that such correlation should also hold for sooting lab-scale flames as long as gas emission is significant, resulting in a strong domination of gas absorption. This is illustrated in Fig. 10 which includes all the data for which gas emission is higher or comparable to soot emission. In particular all the data for ethylene are considered. Figure 10 confirms that, although the correlation obtained for ‘non luminous flames is less representative of the ethylene and acetylene data, it can be used to describe flame self-absorption for lab-scale moderately sooting flames.

3.3.4. Discussions

Equation 3 shows that the radiant fraction depends on the residence time, on the total gas and soot emission per unit flame volume and on the flame ‘transparency’, $1 - \dot{Q}_{abs}/\dot{Q}_{em}$. The reduction of the radiant fraction as the exit strain rates increases is due to the two mechanisms described in section 3.3.2 and 3.3.3. The first mechanism is a decrease in flame transparency owing to an enhancement in flame size. The second mechanism, that affects the sooting ethylene and acetylene flames, is related to a strong decrease in soot emission per unit flame volume.

3.3.5. Turbulence-radiation interaction (TRI)

This section investigates the effects of TRI on predicted radiant fraction. When TRI is disregarded (NoTRI), both total emission and absorption terms are simply evaluated based on mean species mole fraction, soot volume fraction and temperature, i.e. $\dot{Q}_{em,NoTRI} = \int_{V_f} 4\pi\kappa_p(\langle x_i \rangle, \langle f_S \rangle, \langle T \rangle) I_b(\langle T \rangle) dV$ and $\dot{Q}_{abs,NoTRI} = \int_{V_f} \int_{\eta} \kappa_{\eta}(\langle x_i \rangle, \langle f_S \rangle, \langle T \rangle) \langle G_{\eta} \rangle d\eta dV$. It

should be pointed out that $\dot{Q}_{em,NoTRI}$ and $\dot{Q}_{abs,NoTRI}$ were determined from decoupled radiation calculation by using quantities computed with the complete CFD simulation (including TRI), i.e. without considering the feedback of disregarding TRI on the thermal input.

Figures 11 a and b show that the evolutions $(\chi_R)_{TRI}/(\chi_R)_{NoTRI}$ and $(\dot{Q}_{em})_{TRI}/(\dot{Q}_{em})_{NoTRI}$ as a function of the exit strain rate are very similar. This demonstrates that TRI effects on radiant fraction result mainly from effects on total emission [19].

The local gas and soot emission TRI terms can be developed as [40]:

$$\begin{aligned} \langle \kappa_p I_b \rangle \approx & \underbrace{\kappa_p(\langle \phi \rangle) I_b(\langle T \rangle)}_{\langle \kappa_p I_b \rangle_{NoTRI}} + \underbrace{[\langle \kappa_p \rangle - \kappa_p(\langle \phi \rangle)] I_b(\langle T \rangle)}_I + \underbrace{\langle \kappa_p \rangle \left(\frac{\partial^2 I_b}{\partial T^2} \right)_{\langle T \rangle} \frac{\langle T'^2 \rangle}{2}}_{II} \\ & + \underbrace{\left(\frac{\partial I_b}{\partial T} \right)_{\langle T \rangle} \langle \kappa_p' T' \rangle}_{III} \end{aligned} \quad (7)$$

TRI contributes to emission through the last three terms in Eq. (7). Terms I, II, and III quantify the effects of the Planck-mean absorption coefficient self-correlation, of the temperature self-correlation, and of the cross-correlation between Planck-mean absorption coefficient and temperature, respectively [41]. The three contributions tend to enhance gas emission [15, 19, 21]. On the other hand, term II tends to enhance soot emission whereas terms I and III tend to reduce it due to the negative correlation between temperature and the soot Planck-mean absorption coefficient in regions of soot emission [23]. This correlation evolves as the cross-correlation between temperature and soot volume fraction which was observed to be negative in both experimental [42-45] and numerical [23, 46, 47] investigations of turbulent diffusion flames. This negative behavior is illustrated in Figs. 11 c, d, and e for methane, ethylene, and acetylene flames, respectively. The reducing effects of this

correlation on soot emission TRI were found to be enhanced with both the fuel sooting propensity and the Reynolds number (and exit strain rate, U_F/d_F) [23]. As a consequence, the effects of TRI on total emission and radiant fraction result from a competition between mechanisms that tend to enhance them, i.e. gas emission TRI and temperature self-correlation effects on soot emission TRI, and mechanisms that tend to reduce them, i.e. the negative correlation between soot volume fraction and temperature that affects terms I and III in the soot emission term. The competition between these mechanisms evolves with the fuel sooting propensity and the Reynolds number (exit strain rate, U_F/d_F).

The low-sooting methane flames are dominated by gas radiation (see Fig. 5 a₁), and naturally considering TRI enhances both the total emission and radiant fraction in these flames (see Figs. 11 a and b).

On the other hand, the high-sooting acetylene flames are on the whole dominated by soot radiation (see Fig. 5 c₁). For most of these flames, terms I and III prevail on term II in the soot emission term, explaining that $(\chi_R)_{TRI}/(\chi_R)_{NoTRI}$ and $(\dot{Q}_{em})_{TRI}/(\dot{Q}_{em})_{NoTRI}$ are mainly lower than 1 (see Figs. 11 a and b). Based on the previous discussion, the non-monotonic evolution of both $(\chi_R)_{TRI}/(\chi_R)_{NoTRI}$ and $(\dot{Q}_{em})_{TRI}/(\dot{Q}_{em})_{NoTRI}$ with U_F/d_F observed for the acetylene flames can be explained as follows: at low values of U_F/d_F soot radiation dominates (see Fig. 5c₁) and increasing U_F/d_F (i.e. the Reynolds number) tends to enhance the effects of the negative correlation between the soot volume fraction and temperature and, therefore, to reduce $(\chi_R)_{TRI}/(\chi_R)_{NoTRI}$ and $(\dot{Q}_{em})_{TRI}/(\dot{Q}_{em})_{NoTRI}$. After the inflection point, soot radiation becomes less and less important as U_F/d_F increases (see Fig. 5 c₁) and both $(\chi_R)_{TRI}/(\chi_R)_{NoTRI}$ and $(\dot{Q}_{em})_{TRI}/(\dot{Q}_{em})_{NoTRI}$ increase.

$(\chi_R)_{TRI}/(\chi_R)_{NoTRI}$ and $(\dot{Q}_{em})_{TRI}/(\dot{Q}_{em})_{NoTRI}$ evolves with U_F/d_F in the ethylene flames in a similar manner as in the acetylene flames. Nevertheless, for the ethylene flames, $(\chi_R)_{TRI}/(\chi_R)_{NoTRI}$ and $(\dot{Q}_{em})_{TRI}/(\dot{Q}_{em})_{NoTRI}$ are higher than 1, showing that the TRI mechanisms responsible for an enhancement in emission dominate those responsible for a reduction.

4. Concluding remarks

The radiative structure of methane, ethylene and acetylene lab-scale jet fires were numerically investigated by using a RANS hybrid flamelet/transported PDF method coupled to an acetylene-benzene soot production model and a WBCK gas radiation model. The following conclusions can be drawn:

- 1) Model predictions in terms of mean and rms soot volume fraction and temperature, integrated soot volume fraction and radiant fraction are in reasonable agreement with the available experimental data.
- 2) The radiant fraction depends on three terms: i) a global residence time, ii) the total emission of gas and soot per unit flame volume, and iii) the flame transparency.
- 3) None of the flames investigated in this study can be considered as optically-thin. The flame optical thickness, defined as the ratio of total absorption to total emission, increases with the exit strain rate due to an increase in flame size. In the case of weakly and moderately sooting flames, it is found to correlate with the gas-phase Planck-mean absorption coefficient, evaluated based on an adiabatic flame temperature and an equilibrium composition, and the flame width.
- 4) Gas emission per unit flame volume remains approximately constant when increasing the exit strain rate whereas soot emission per unit flame volume decreases significantly due a strong reduction in soot production. Soot emission per unit volume and characteristic soot

volume fraction scale with the Kolmogorov time scale, supporting that it is the characteristic time scale for soot production.

5) The effects of TRI on radiant fraction results from a competition between enhancement mechanisms, i.e. gas emission TRI and temperature self-correlation effects on soot emission, and inhibiting mechanisms, i.e. the negative correlation between soot volume fraction and temperature that reduces soot emission. The first mechanisms dominate in the weakly sooting methane flames whereas the second becomes significant in moderately and highly sooting fuels, with their importance increasing with both the fuel sooting propensity and the Reynold number. For flames dominated by soot radiation, the second mechanisms prevails and taking TRI into account reduces the radiation fraction.

References

- [1] J.P. Gore, G.M. Faeth, D. Evans, D. B. Pfenning, Structure and radiation properties of large-scale natural gas/air diffusion flames, *Fire Materials* 10 (1986) 161-169.
- [2] J.P. Gore, G.M. Faeth, Structure and spectral radiation properties of turbulent ethylene/ air diffusion flames, *Proc. Combust. Inst.* 21 (1988) 1521-1531.
- [3] M.A. Delichatsios, L. Orloff, Effects of turbulence on flame radiation from diffusion flames, *Proc. Combust. Inst.* 22 (1989) 1271-79.
- [4] G.M. Faeth, J.P. Gore, S.G. Chuech, S.M. Jeng, Radiation from turbulent diffusion flames, *Annual Review Heat Transf.* 2 (1989) 1-38.
- [5] S.R. Turns, F.H. Myhr, Oxides of nitrogen emissions from turbulent jet flames: Part I— Fuel effects and flame radiation, *Combust. Flame* 87 (1991) 319-35.
- [6] Y.R. Sivathanu, J.P. Gore, Total radiative heat loss in jet flames from single point radiative flux measurements, *Combust. Flame* 94 (1993) 265-70.

- [7] L. Wang, N.E. Endrud, S.R. Turns, M. D. D'Agostini, A. G. Slavejkov, A study of the influence of oxygen index on soot, radiation, and emission characteristics of turbulent jet flames, *Combust. Sci. Technol.* 174 (2002) 45-72.
- [8] R.W. Schefer, W.G. Houf, B. Bourne, J. Colton, *Int. J. Hydrogen Energ.* 31 (2006) 1332-40.
- [9] R.W. Schefer, W.G. Houf, T.C. Williams, B. Bourne, J. Colton, Spatial and radiative properties of an open-flame hydrogen plume, *Int. J. Hydrogen Energ.* 32 (2007) 2081-93.
- [10] A. Molina, R.W. Schefer, W.G. Houf, Radiative fraction and optical thickness in large- scale hydrogen-jet fires, *Proc. Combust. Inst.* 31 (2007) 2565-72.
- [11] J.L. Consalvi, F. Nmira, Modeling of large-scale under-expanded hydrogen jet fires, *Proc. Combust. Inst.* 37 (2019) 3943-3950.
- [12] M.F. Modest, D.C. Haworth, *Radiative Heat Transfer in Turbulent Combustion Systems: Theory and Applications*, Springer, 2016.
- [13] L.S. Rothman, I.E. Gordon, R.J. Barber, H. Dothe, R.R. Gamache, A. Goldman, V.I. Perevalov, S.A. Tashkun, J. Tennyson, HITEMP, the high-temperature molecular spectroscopic database, *J. Quant. Spectrosc. Radiat. Transf.* 111 (2010) 2139-50.
- [14] M. F. Modest, *Radiative Heat Transfer*, Third ed., Academic Press, New York, 2013.
- [15] A. Wang, M.F. Modest, D.C. Haworth, L. Wang, Monte Carlo simulation of radiative heat transfer and turbulence interactions in methane/air jet flames, *J. Quant. Spectrosc. Radiat. Transf.* 109 (2008) 269-79.
- [16] R.S. Mehta, M.F. Modest, D.C. Haworth, Radiation characteristics and turbulence–radiation interactions in sooting turbulent jet flames, *Combust. Theory Model.* 14 (2010) 105-24.
- [17] P.J. Coelho, Detailed numerical simulation of radiative transfer in a nonluminous turbulent jet diffusion flame, *Combust. Flame* 136 (2004) 481-92.

- [18] P.J. Coelho, O.J. Teerling, D. Roekaerts, Spectral radiative effects and turbulence/radiation interaction in a non-luminous turbulent jet diffusion flame, *Combust. Flame* 133 (2003) 75-91.
- [19] G. Li, M.F. Modest, Investigation of turbulence–radiation interactions in reacting flows using a hybrid FV/PDF Monte Carlo method, *J. Quant. Spectrosc. Radiat. Trans.* 73 (2002) 461-72.
- [20] R.S. Metha, D.C. Haworth, M.F. Modest, Composition PDF/photon Monte Carlo modeling of moderately sooting turbulent jet flames, *Combust. Flame* 157 (2010) 982-94.
- [21] J.L. Consalvi, Influence of turbulence–radiation interactions in laboratory-scale methane pool fires, *Int. J. Thermal Sci.* 2012; 60: 122-30.
- [22] J.L. Consalvi, F. Nmira, Absorption turbulence-radiation interactions in sooting turbulent jet flames, *J. Quant. Spectrosc. Radiat. Transf.* 201 (2017) 1-9.
- [23] F. Nmira, D. Burot, J.L. Consalvi, Soot emission radiation–turbulence interactions in diffusion jet flames, *Combust. Sci. Technol.* 191 (2019) 136-136.
- [24] J.L. Consalvi, F. Nmira, D. Burot, Simulations of sooting turbulent jet flames using a hybrid flamelet/stochastic Eulerian field method, *Combust. Theor. Model.* 20 (2016) 221-57.
- [25] J.L. Consalvi, F. Nmira, Transported Scalar PDF Modelling of Oxygen-Enriched Turbulent Jet Diffusion Flames: Soot Production and Radiative Heat Transfer, *Fuel* 178 (2016) 37–48
- [26] Z. Qin, V.V. Lissianski, H. Yang, W.C. Gardiner, S.G. Scott SG, H. Wang, Combustion chemistry of propane: a case study of detailed reaction mechanism optimization, *Proc. Combust. Inst.* 28 (2000) 1663-69.
- [27] R.P. Lindstedt, Simplified Soot Nucleation and Surface Growth Steps for Non-Premixed Flames, in: Bockhorn H (Eds.), *Soot Formation in Combustion: Mechanism and Models*, Springer-Verlag, Berlin, 1994, p. 417-441.

- [28] J. Naggle, R.F. Strickland-Constable, Oxidation of carbon between 1000-2000°C, Proc. 5th conference on carbon, London: Pergamon Press, pp. 154-164, 1962.
- [29] C.P. Fenimore, G. W. Jones, Oxidation of soot by hydroxyl radicals, J. Phys. Chem. 71 (1967) 593-97.
- [30] H. Chang, T. Charalampopoulos, Determination of the wavelength dependence of refractive indices of flame soot, Proc. R. Soc. 430 (1990) 577-91.
- [31] H. Chu, J.L. Consalvi, M. Gu, F. Liu, Calculations of radiative heat transfer in an axisymmetric jet diffusion flame at elevated pressures using different gas radiation models, J. Quant. Spectrosc. Radiat. Transf. 197 (2017) 12-25.
- [32] M.F. Modest, R.J. Riazzi, Assembly full spectrum k-distribution from a narrow band database: effects of mixing gases, gases and non-gray absorbing particles and non-gray scatters in non-gray enclosures, J. Quant. Spectrosc. Radiat. Transf. 90 (2005) 169-89.
- [33] E.H. Chui, G.D. Raithby, P.M.J. Hughes, Prediction of radiative transfer in cylindrical enclosures with the finite volume method, J. Thermophys. Heat Transf. 6 (1992) 605-11.
- [34] L. Valiño, A field Monte Carlo formulation for calculating the probability density function of a single scalar in a turbulent flow, Flow Turb. Combust. 29 (1998) 2139-46.
- [35] G.H. Markstein, J. De Ris, Radiant emission and absorption by laminar ethylene and propylene diffusion flames, Proc. Combust. Inst. 20 (1985) 1637-46.
- [36] J.H. Kent, A quantitative relationship between soot yield and smoke point measurements, Combust. Flame 63 (1986) 349-58.
- [37] M.A. Delichatsios, Transition from momentum to buoyancy-controlled turbulent jet diffusion flames and flame height relationships, Combust. Flame 156 (1993) 349-64.
- [38] S.Y. Lee, S.R. Turns, R.J. Santoro, Measurements of soot, OH, and PAH concentrations in turbulent ethylene/air jet flames, Combust. Flame 156 (2009) 2264-75.
- [39] S.M. Mahmoud, G.J. Nathan, Z.T. Alwahas, Z.W. Sun, P.R. Medwell, B.B. Dally,

The effect of exit Reynolds number on soot volume fraction in turbulent non-premixed jet flames, *Combust. Flame* 187 (2018) 42–51.

- [40] M.A. Delichatsios, L. Orloff, M.M. Delichatsios, The effects of fuel sooting tendency and the flow on flame radiation in luminous turbulent jet flames, *Combust. Sci. Technol.* 84 (1992) 199-215.
- [41] P.J. Coelho, Numerical simulation of the interaction between turbulence and radiation in reactive flows, *Prog. Energy Combust. Sci.* 33 (2007) 311-383.
- [42] Y.R. Sivathanu, J.P. Gore, J. Dolinear, Transient scalar properties of strongly radiating jet flames, *Combust. Sci. and Tech.* 76 (1991) 45-66.
- [43] Y.R. Sivathanu, J.P. Gore, Transient structure and radiation properties of strongly radiating buoyant flames, *J. Heat Transf.* 114 (1992) 659-665.
- [44] J.J. Murphy, C.R. Shaddix, Soot properties and species measurements in a two-meter diameter JP-8 pool fire, Sandia Report, SAND20034246, 2003.
- [45] D. Zeng, P. Chatterjee, Y. Wang, The effect of oxygen depletion on soot and thermal radiation in buoyant turbulent diffusion flames, *Proc. Combust. Inst.* 37 (2019) 825–832.
- [46] W. Kollmann, I.M. Kennedy, M. Metternich, J.Y. Chen, “Application of a soot model to a turbulent ethylene diffusion flame”, in: Bockhorn H (Eds.), *Soot Formation in Combustion: Mechanism and Models*, Springer-Verlag, Berlin, 1994, pp. 503-526.
- [47] J.L. Consalvi, F. Nmira, Effects of soot absorption coefficient–Planck function correlation on radiative heat transfer in oxygen-enriched propane turbulent diffusion flame, *J. Quant Spectrosc. Radiat Transf.* 172 (2016) 50-57.

Table 1. Rate expressions for the soot production model.

Process	Rate
Nucleation	$\dot{\omega}_n = 2k_1[C_2H_2] + 6k_2[C_6H_6]$
Surface growth	$\dot{\omega}_{sg} = 2k_3[C_2H_2]A_s$
Oxidation O ₂	$\dot{\omega}_{O_2} = 120 \left[\frac{k_a P_{O_2} \chi}{1 + k_z P_{O_2}} + (1 - \chi)k_b P_{O_2} \right] A_s$
Oxidation OH	$\dot{\omega}_{OH} = 1.27 \times 10^3 \varphi_{OH} \frac{P_{OH}}{\sqrt{T}} A_s$
Coagulation	$\dot{\omega}_c = 2C_a \left(\frac{6W_s}{\pi\rho_s} \right)^{1/6} \left(\frac{6k_B T}{\rho_s} \right)^{1/2} \left(\frac{\rho Y_s}{W_s} \right)^{1/6} (\rho N_s)^{11/6}$

$C_a = 9$ [26]; $C_{min} = 60$ [27]; $\varphi_{OH} = 0.06$ [24]; $k_1 = 0.63 \times 10^4 \exp(-21000/T)$ [27], $k_2 = 0.75 \times 10^4 \exp(-21000/T)$ [27]; $k_3 = 0.4 \times 10^3 \exp(-12100/T)$ [24]. $A_s = \pi \left(\frac{6W_s}{\pi\rho_s} \right)^{2/3} \left(\frac{\rho Y_s}{W_s} \right)^{2/3} (\rho N_s)^{1/3}$; soot surface per unit volume of mixture. The expression of k_a , k_b , k_z , χ for the NCS model can be found in Ref. [28].

Table 2. Flame conditions.

Fuel	d_F (mm)	U_F (mm)	U_F/d_F $\times 10^4$ (s ⁻¹)	Re^a $\times 10^3$ (-)	\dot{Q}^b (kW)	Fr^c (-)	t_{Kol} $\times 10^6$ (s)
CH ₄	1	100-250	10-25	5.67-14.2	2.64-6.6	5.93-14.83	2.48-0.63
	2	32.5-200	1.63-10	3.69-22.7	3.43-21.1	1.36-8.39	14.9-1.19
	3	32.5-140	1.08-4.67	5.53-23.8	7.72-33.3	1.11-4.79	17.7-2.33
C ₂ H ₄	1	50-250	5.00-25.0	5.66-28.3	2.11-10.6	3.14-15.75	4.66-0.49
	2.18 ^d	16.2-140	0.74-6.42	4.00-34.6	3.25-28.1	0.69-5.97	27.0-1.48
	3	15-100	0.50-3.33	5.10-34.0	5.70-38.0	0.54-3.63	34.4-2.63
C ₂ H ₂	1	50-250	5.00-25.0	5.05-25.2	2.00-10.0	3.56-17.80	1.33-0.17
	2	16.2-220	0.74-10.1	3.57-48.4	3.09-41.9	0.78-10.61	7.86-0.64
	3	50-250	1.67-8.33	15.1-75.7	18.0-90.0	2.05-10.28	2.10-0.27

^a $Re = \frac{\rho_F U_F d_F}{\mu_F}$ where ρ_F and μ_F are the cold fuel density and kinematic viscosity, respectively.

^b $\dot{Q} = \rho_F U_F \pi d_F^2 / 4$.

^c $Fr = \frac{U_F Z_{st}^{1.5}}{\left[\left(\frac{\rho_F}{\rho_{ox}} \right)^{0.25} \left(\frac{T_{ad} - T_{ox}}{T_{ox}} g D_F \right)^{0.5} \right]}$ where Z_{st} is the stoichiometric mixture fraction and the subscript *ox*

refers to the oxidizer [37].

^d These injection conditions are similar to those considered by Lee et al. [38].

List of figure captions

Figure 1. Axial profiles of a) mean and b) rms soot volume fractions for the ethylene flames with a nozzle diameter of 2.18 mm and exit Reynolds number of 12,000, 19,100 and 23,200.

The experimental data are taken from Ref. [38].

Figure 2. Radial profiles of mean soot volume fraction at different heights for the ethylene flames with a nozzle diameter of 2.18 mm and Reynolds number of a) 8,000, b) 12,000 and c) 19,100. The experimental data are taken from Ref. [38].

The experimental data are taken from Ref. [38].

Figure 3. Integrated soot volume fraction for the ethylene flames with a nozzle diameter of 2.18 mm and different Reynolds numbers. The experimental data are taken from Ref. [38].

Figure 4. Radiant fraction as a function of the heat release rate (index 1) or U_F/d_F (index 2): a) the methane flames, b) the ethylene flames and c) the acetylene flames. The experimental data are taken from Ref. [3].

Figure 5. Total emission of gas and soot per unit flame volume rate (index 1) and equivalent soot volume fraction (index 2) as a function of U_F/d_F : a) the methane flames, b) the ethylene flames and c) the acetylene flames.

Figure 6. Total emission of soot per unit flame volume rate as a function of the equivalent soot volume fraction.

Figure 7. Total emission of soot per unit flame volume rate as a function of Kolmogorov time scale.

Figure 8. Ratio of the emission fraction to the global residence time as a function of the Kolmogorov time scale for: a) methane flames, b) ethylene flames and c) acetylene flames.

Figure 9. $\dot{Q}_{abs}/\dot{Q}_{em}$ as a function of U_F/d_F for: a) methane flames, b) ethylene flames and c) acetylene flames.

Figure 10. Computed $\dot{Q}_{abs}/\dot{Q}_{em}$ as a function of $\kappa_{pg,Eq}W_{fl}$. The diamonds and gradient symbols correspond to the numerical simulations reported in Ref. [11] of the lab-scale H₂ and CH₄ flames investigated experimentally in Refs. [8] and [9], respectively.

Figure 11. Effects of TRI on radiant fraction. a) Ratio of the radiant fraction computed with TRI to the radiant fraction computed without TRI as a function of U_F/d_F , b) Ratio of the total emission computed with TRI to total emission computed without TRI as a function of U_F/d_F . In the diagrams a) and b) the horizontal dashed lines corresponds to a ratio of 1. Diagrams c), d) and e) Axial cross-correlation between soot volume fraction and temperature,

defined as $C(f_S, T) = \frac{\overline{f_S' T'}}{\sqrt{\overline{f_S'^2} \sqrt{\overline{T'^2}}}$, for a 15kW-methane flame diameter (c), a 16kW-ethylene

flame (d) and a 15-kW acetylene flame. Flames in c), d) and e) were generated from a 2 mm-nozzle diameter.

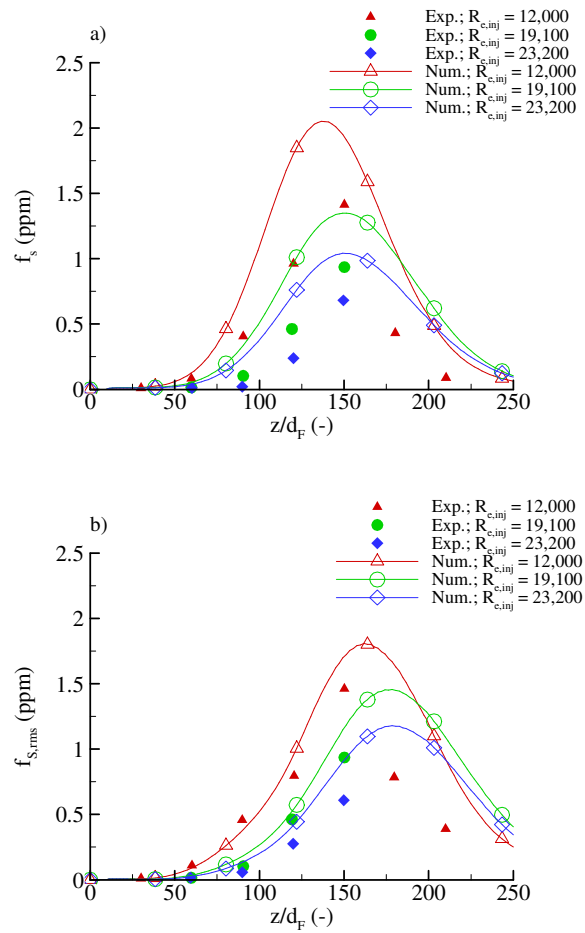


Figure 1. Axial profiles of a) mean and b) rms soot volume fractions for ethylene flames with a nozzle diameter of 2.18 mm and exit Reynolds number of 12,000, 19,100 and 23,200. The experimental data are taken from Ref. [38].

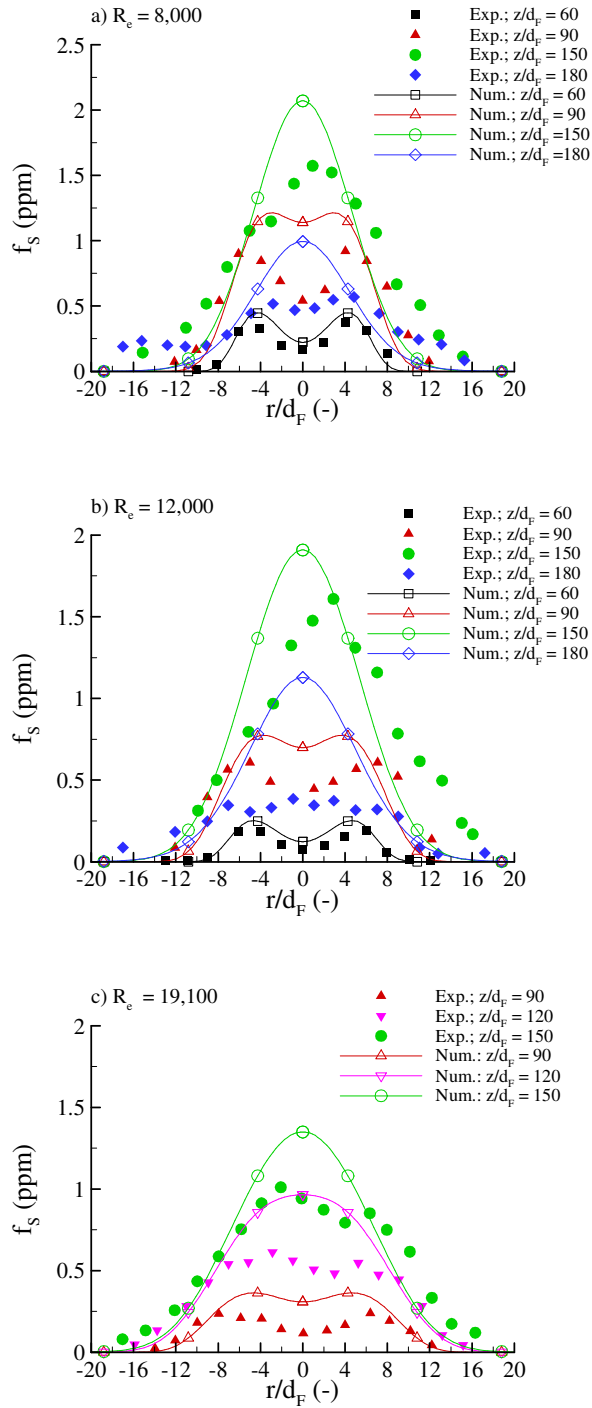


Figure 2. Radial profiles of mean soot volume fraction at different heights for the ethylene flames with a nozzle diameter of 2.18 mm and Reynolds number of a) 8,000, b) 12,000 and c) 19,100. The experimental data are taken from Ref. [38].

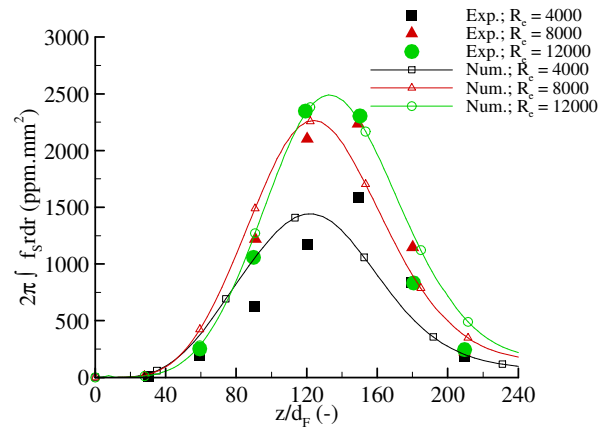


Figure 3. Integrated soot volume fraction for the ethylene flames with a nozzle diameter of 2.18 mm and different Reynolds numbers. The experimental data are taken from Ref. [38].

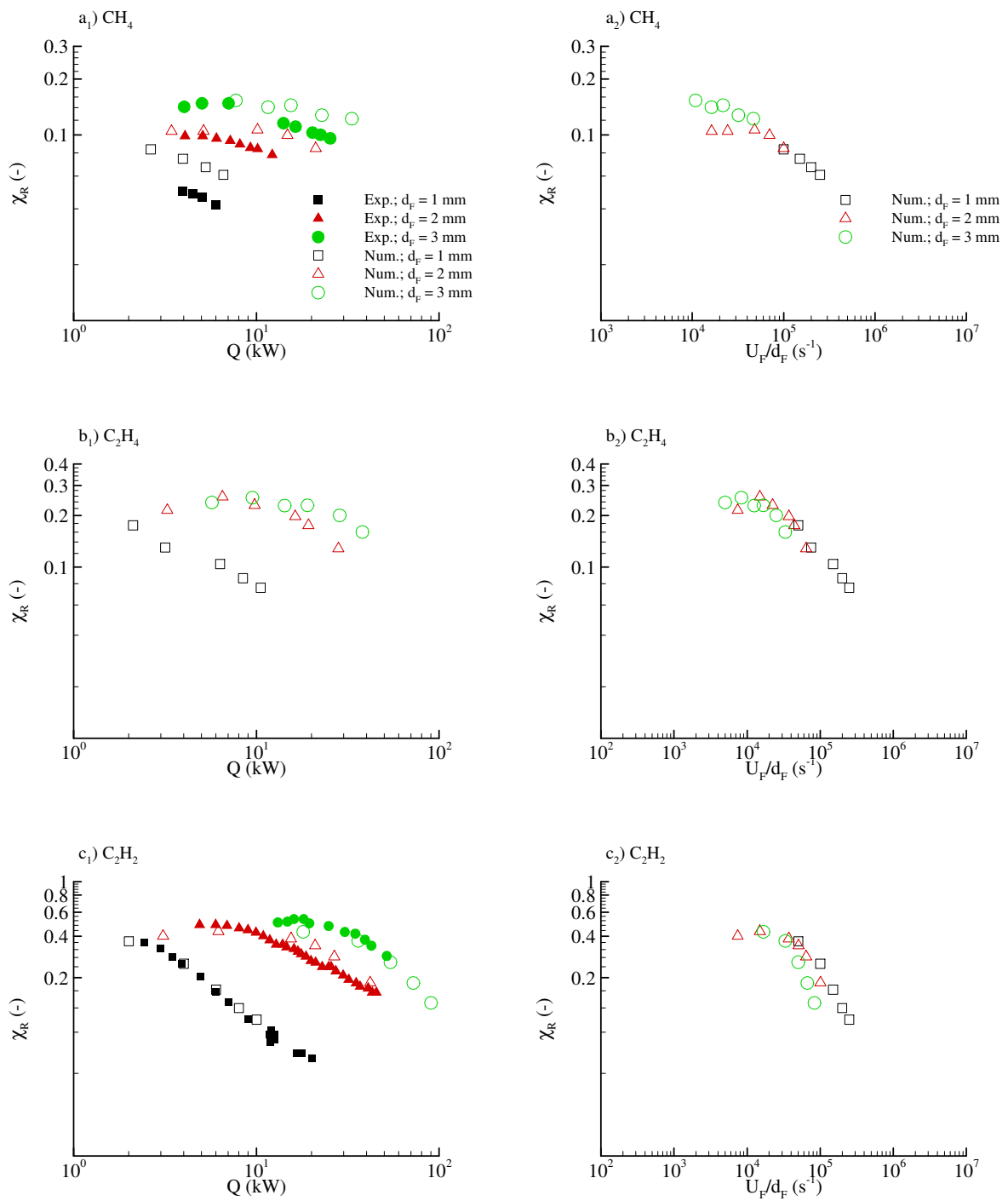


Figure 4. Radiant fraction as a function of the heat release rate (index 1) or U_F/d_F (index 2): a) the methane flames, b) the ethylene flames and c) the acetylene flames. The experimental data are taken from Ref. [3].

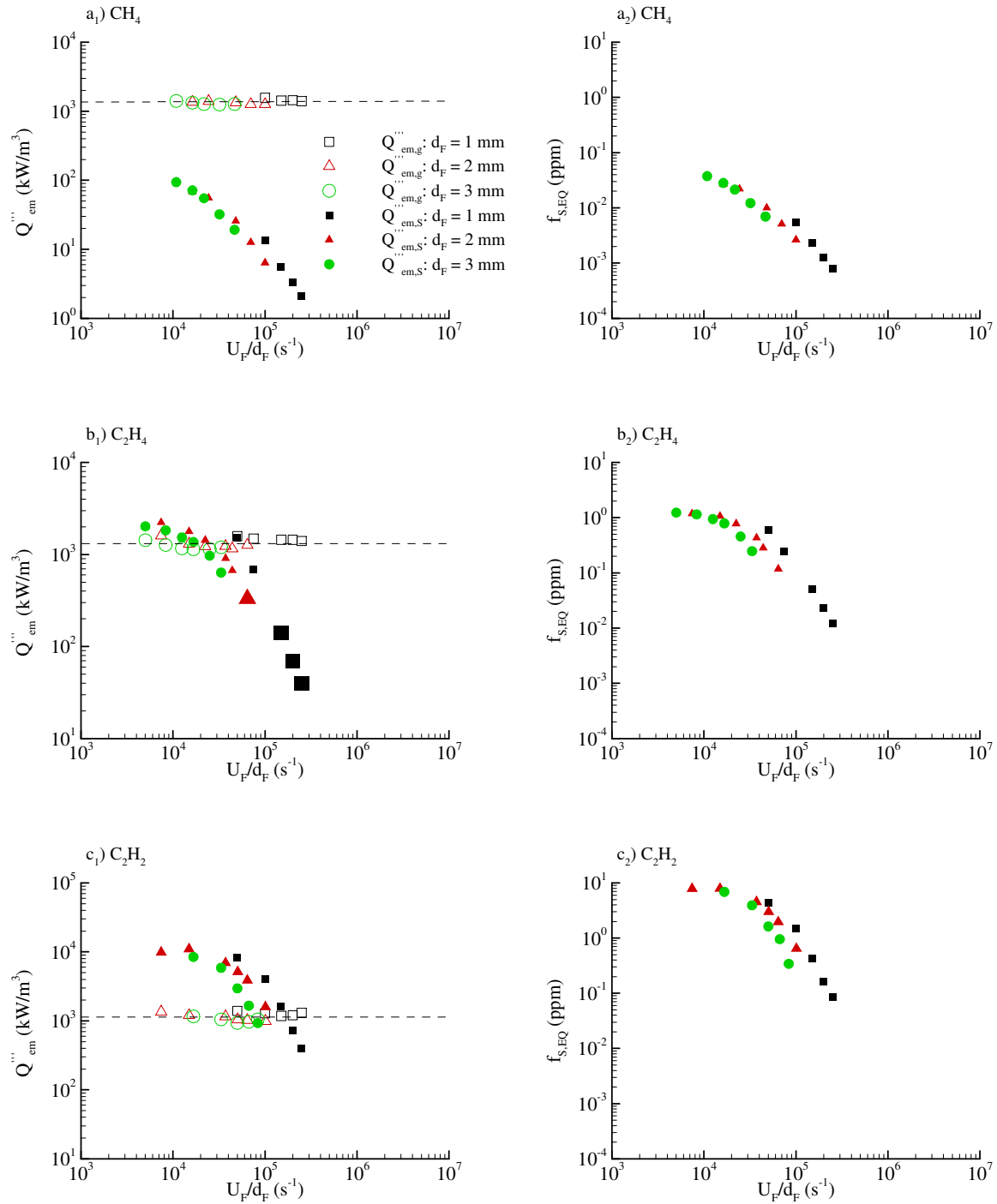


Figure 5. Total emission of gas and soot per unit flame volume rate (index 1) and equivalent soot volume fraction (index 2) as a function of U_F/d_F : a) the methane flames, b) the ethylene flames and c) the acetylene flames. The horizontal dashed line indicates the mean total emission of gas.

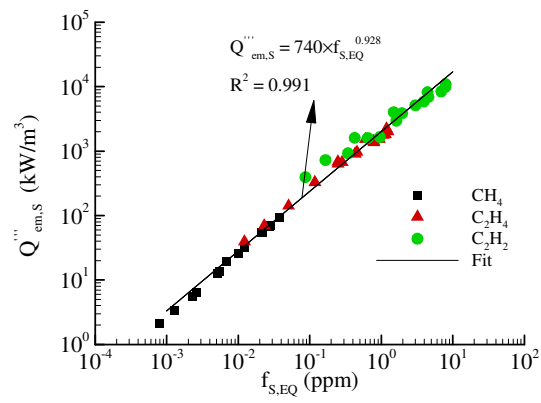


Figure 6. Total emission of soot per unit flame volume rate as a function of the equivalent soot volume fraction.

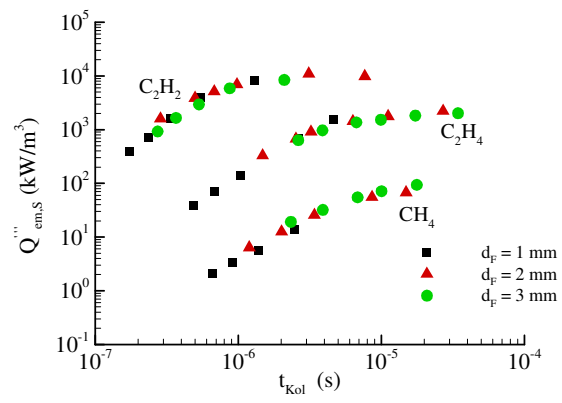


Figure 7. Total emission of soot per unit flame volume rate as a function of Kolmogorov time scale.

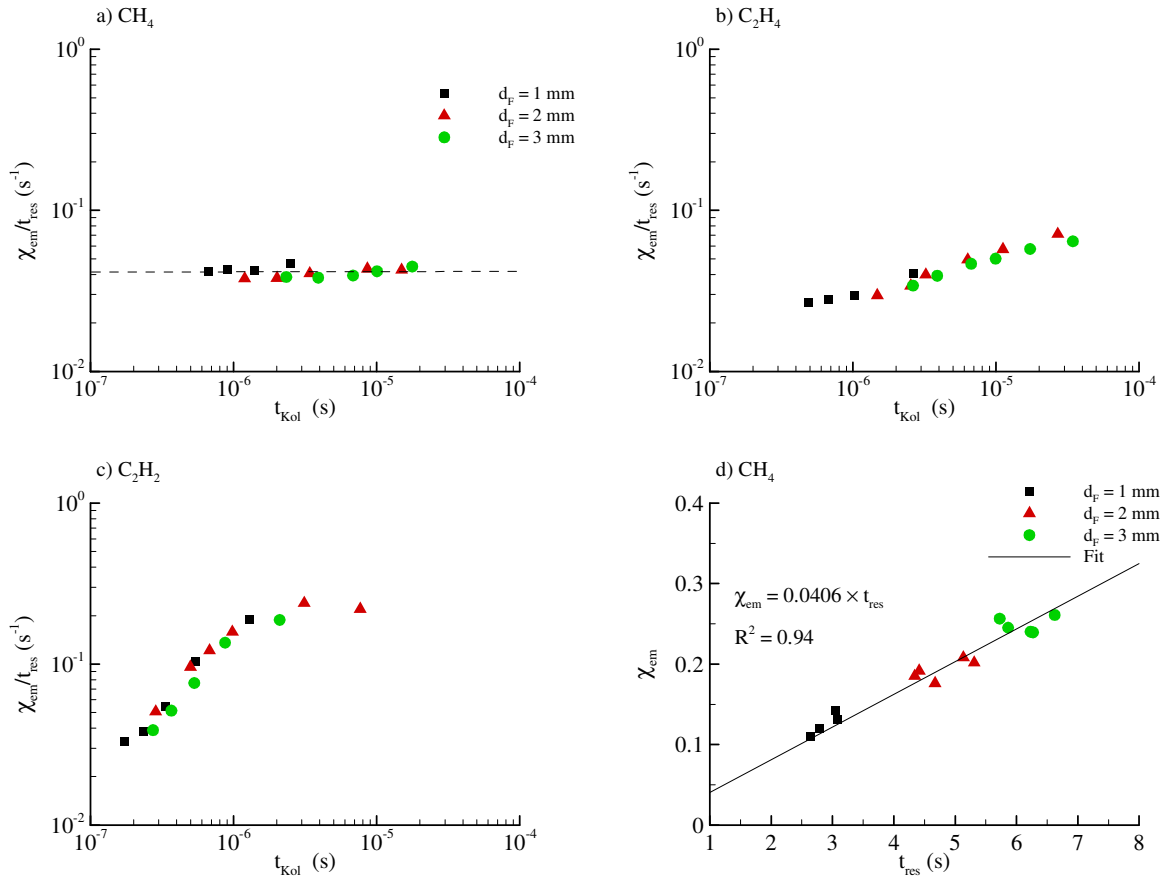


Figure 8. Ratio of the emission fraction to the global residence time as a function of the Kolmogorov time scale for: a) methane flames, b) ethylene flames and c) acetylene flames, d) emission fraction as a function of the global residence time for the methane flames.

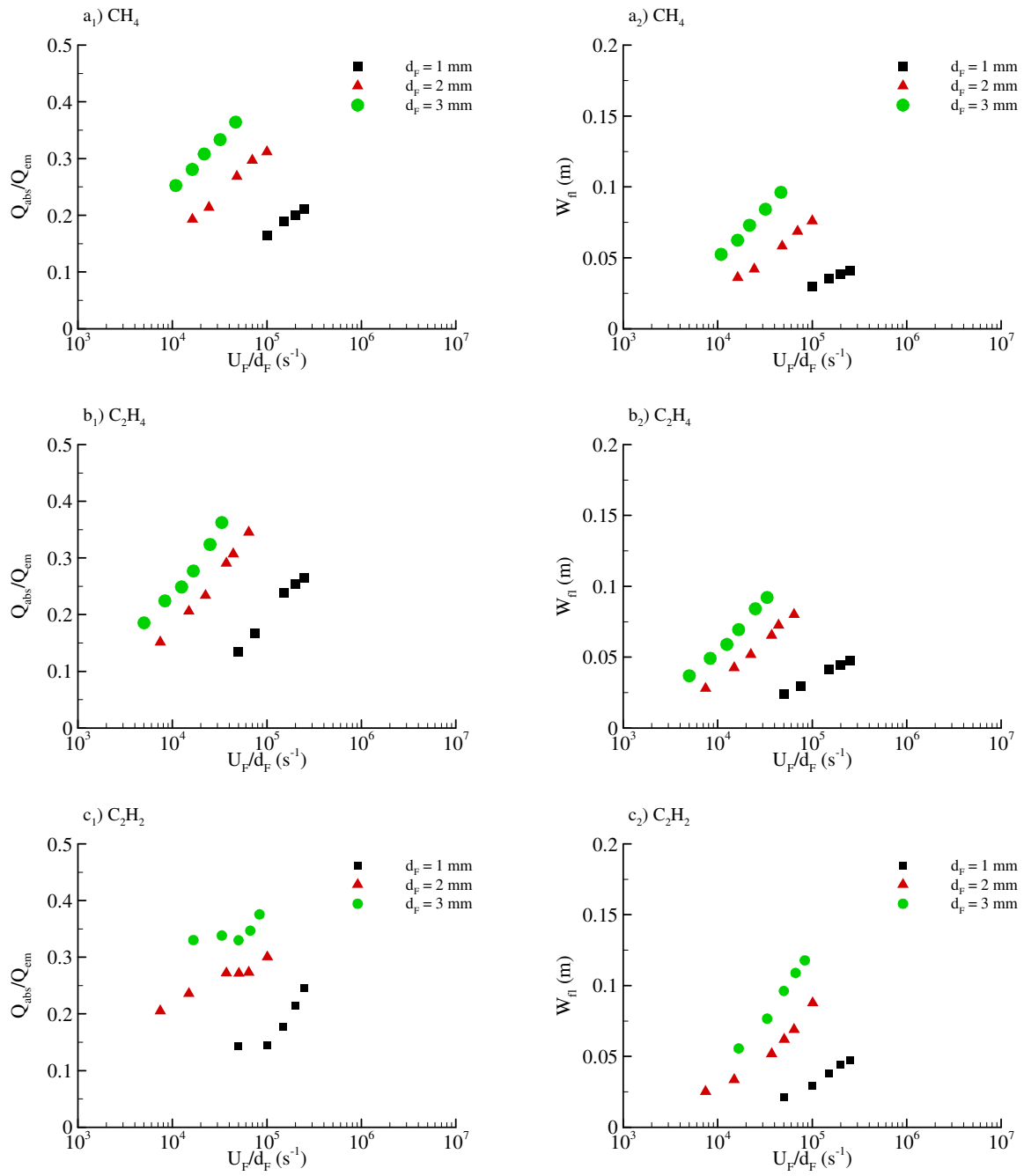


Figure 9. $\dot{Q}_{abs}/\dot{Q}_{em}$ (index 1) and W_{fl} (index 2) as a function of U_F/d_F for: a) methane flames, b) ethylene flames and c) acetylene flames.

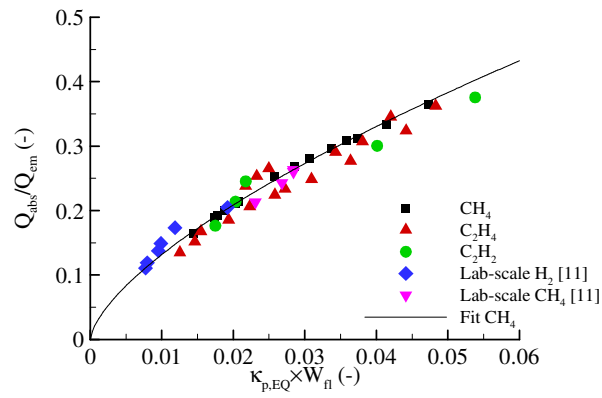


Figure 10. Computed $\dot{Q}_{abs}/\dot{Q}_{em}$ as a function of $\kappa_{pg,Eq}W_{fl}$. The diamonds and gradient symbols correspond to the numerical simulations reported in Ref. [11] of the lab-scale H₂ and CH₄ flames investigated experimentally in Refs. [8] and [9], respectively. Note that the definition of the flame width for these flames was modified from Ref. [11] to be consistent with that adopted in this study.

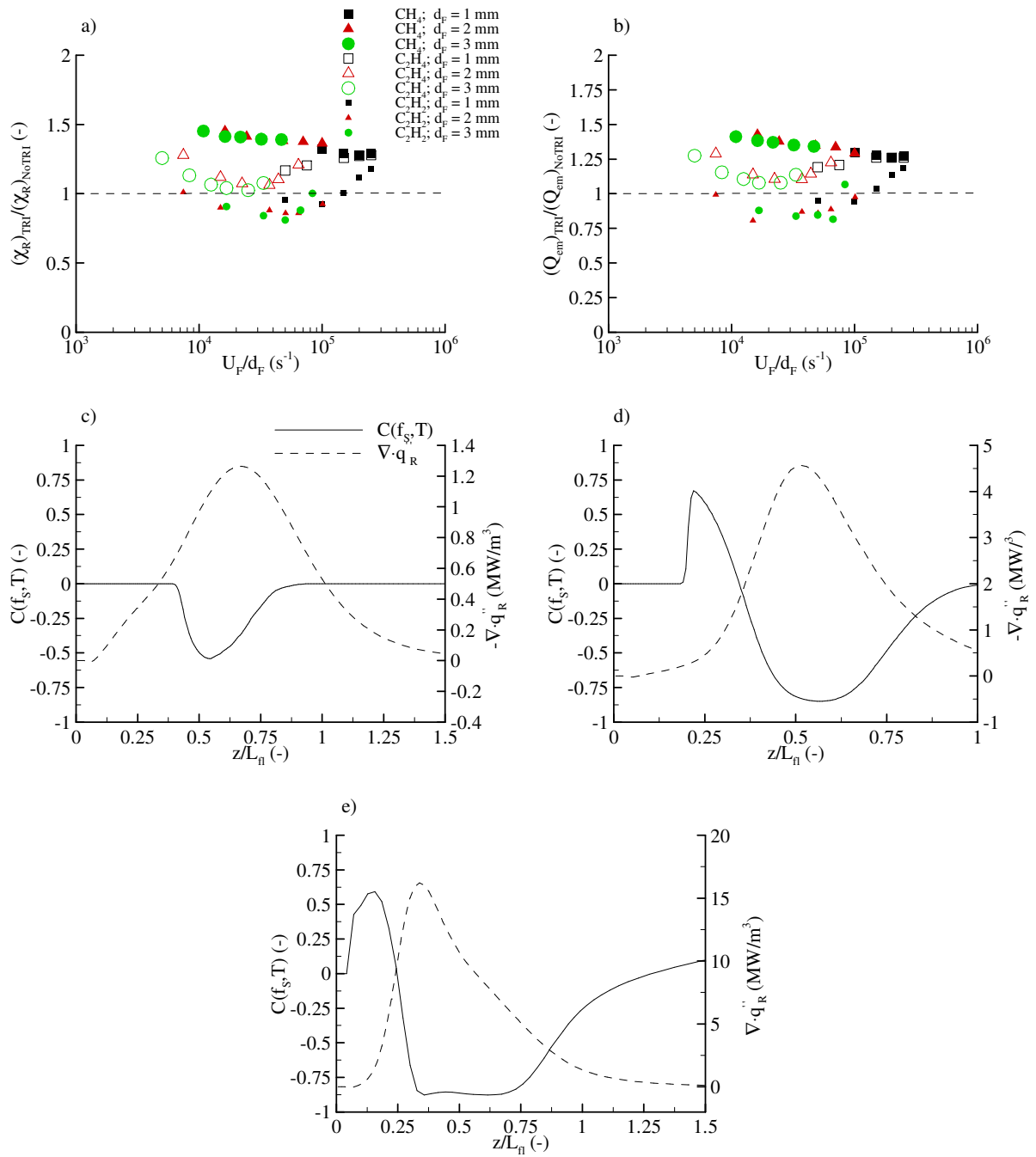


Figure 11. Effects of TRI. a) Ratio of the radiant fraction computed with TRI to the radiant fraction computed without TRI as a function of U_F/d_F , b) Ratio of the total emission computed with TRI to total emission computed without TRI as a function of U_F/d_F . In the diagrams a) and b) the horizontal dashed lines corresponds to a ratio of 1. Diagrams c), d) and e) Axial cross-correlation between soot volume fraction and temperature, defined as

$$C(f_s, T) = \frac{\overline{f_s T'}}{\sqrt{\overline{f_s'^2} \sqrt{\overline{T'^2}}}, \text{ for a 15kW-methane flame diameter (c), a 16kW-ethylene flame (d) and}$$

a 15-kW acetylene flame. Flames in c), d) and e) were generated from a 2 mm-nozzle diameter.